Miner Deposita (2006) 41: 549–564
DOI 10.1007/s00126-006-0077-3

ARTICLE

Mustapha El Ghorfi · Thomas Oberthür · Frank Melcher · Volker Lüders · Abdelmajid El Boukhari · Lhou Maacha · Rachid Ziadi · Hssain Baoutoul

Gold–palladium mineralization at Bleïda Far West, Bou Azzer–El Graara Inlier, Anti-Atlas, Morocco

Received: 20 December 2005 / Accepted: 12 June 2006 / Published online: 1 August 2006

Abstract The structurally controlled Au–Pd mineralization at Bleïda Far West occurs in a volcano-sedimentary rock sequence in altered amphibolites and chlorite schists of the Neoproterozoic Bou Azzer–El Graara inlier. The Au–Pd mineralization is virtually sulfide-free; instead, gold is associated with hematite, barite, quartz, and calcite. The gold grains are silver- and palladium-bearing (up to 19 wt% Ag and 6.3 wt% Pd) and are intergrown with a distinct suite of mainly Pd-dominated platinum group minerals, namely mertieite-I/isomertieite, merenskyite, keithconnite, kotulskite, palladseite, and sperrylite, defining a Au–Pd–As–Sb–Se–Te chemical signature. Stable isotope and fluid inclusion studies indicate a wide range of fluid compositions with a prominent saline component. In conjunction with the mineral association, oxidizing fluids are indicated, and Au and PGE transport and deposition likely took place by chloride complexes in the epithermal range, at elevated fO_2 and/or low pH. It is still speculative whether the mineralization is late Pan-African (~600–550 Ma) in age, or connected with the Variscan orogeny (~330–300 Ma), or related to some other hydrothermal event. Common to all Au–Pd mineralizations worldwide (Brazil, Australia, UK), including Bleïda Far West, is their formation in the epithermal (<300°C) range; deposition mainly in brittle structures; sulfide-poor mineral assemblages comprising hematite, sulfate minerals, and selenides; and metal transport by, and deposition from, oxidized, chloride-rich fluids. These deposits are further characterized by noble metal abundances in the order Au>Pd>Pt and the chemical signature Au–Pd–Se–Te (±As, Sb, Bi). As such, the Au–Pd association represents a discrete style of gold mineralization distinct from other classes of gold deposits.

Keywords Gold–palladium mineralization · Palladian gold · Platinum group minerals · Bleïda Far West · Anti-Atlas · Morocco

Editorial handling: B. Lehmann

M. El Ghorfi · T. Oberthür · F. Melcher
Federal Institute for Geosciences and Natural Resources (BGR),
Stilleweg 2,
30655 Hannover, Germany
e-mail: thomas.oberthuer@bgr.de

M. El Ghorfi (✉) · A. El Boukhari
Faculty of Sciences Semlalia, Department of Geology,
University Cadi Ayyad,
Marrakech, Morocco
e-mail: must_elghorfi@yahoo.fr

V. Lüders
Geoforschungszentrum Potsdam (GFZ),
Telegrafenberg,
14473 Potsdam, Germany

L. Maacha · R. Ziadi · H. Baoutoul
Reminex Exploration,
Av. Allal al Fassi,
Marrakech, Morocco

Introduction

The Bou Azzer–El Graara inlier of the Anti-Atlas in Morocco is well-known for its vein-type cobalt–arsenide deposits with gold as a by-product, podiform chromitites, and the mined-out SEDEX-type Bleïda copper deposit (Leblanc and Billaud 1978; Leblanc 1981; Mouttaqi and Sagon 1999). Recent geochemical prospecting by Reminex Exploration led to the discovery of significant gold mineralization some 7 km NW of the former Bleïda copper mine. Managem, a subsidiary of the ONA group, intends to start production at the site in 2006 at a planned annual output of 30,000 oz of gold.

Mainly, drill core and limited surface samples from the Bleïda Far West gold mineralization were studied. The present contribution, therefore, focuses on geochemical and mineralogical aspects of the mineralization with the aim of describing the unusual features of this type of virtually sulfide-free gold mineralization, which carries significant palladium contents and associated platinum group minerals. It is also this works objective to constrain the conditions of ore formation to formulate a metallogenetic model for the deposit,

which is hitherto unique for Africa and represents a discrete style of gold mineralization.

Geological setting

The lithostratigraphic–geodynamic framework and development of the Anti-Atlas of Morocco is a controversial topic (e.g., Choubert 1963; Leblanc and Lancelot 1980; Hefferan et al. 1992, 2000, 2002; Saquaque et al. 1989, 1992; Leblanc and Moussine-Pouchkine 1994; Thomas et al. 2004; Levresse et al. 2004; Gasquet et al. 2004, 2005), and work on modern, comprehensive models of crustal evolution and metallogenesis is still in progress. In general, the recently presented reconstruction of the Anti-Atlas by Thomas et al. (2004) and Gasquet et al. (2005), which regards the Anti-Atlas to represent a complex orogenic front that developed at the northern edge of the Eburnian (ca. 2.1–2.0 Ga) West African Craton during Pan-African times, can be followed. In the Anti-Atlas, the Precambrian basement comprises several Paleoproterozoic to Neoproterozoic units (traditionally subdivided into three "systems" (PI, PII, and PIII), which are unconformably overlain by late Ediacaran to Paleozoic rocks. The Precambrian basement crops out in several inliers, whereby the Bou Azzer–El Graara inlier appears to be the structurally most complex part of the whole Anti-Atlas (Gasquet et al. 2005).

Pioneering work on the Bou Azzer–El Graara inlier stems from Choubert (1963) and Leblanc (1981). The latter author described the inlier as a segment of a Pan-African orogenic belt located along the main Anti-Atlas thrust (Fig. 1). The Bou Azzer–El Graara inlier (Fig. 2) nowadays represents a window into the Proterozoic basement surrounded by a discordantly overlying infra-Cambrian to Paleozoic cover sequence. The inlier was divided by Leblanc (1981) into a western oceanic domain and an eastern continental margin domain. The oceanic domain of Bou Azzer is characterized by an ophiolite complex consisting of a basal sequence of serpentinized peridotites, followed by ultrabasic and basic cumulates (layered gabbros), large stocks of quartz diorite, basic lavas, and a mixed volcanic and sedimentary sequence (Leblanc 1981). The continental margin domain of Bleïda–Tachdamt is characterized by a thick, intimately imbricated sequence of sedimentary (70%) and volcanic (30%) rocks (Leblanc 1981). Two Pan-African tectonic events affected the region (Leblanc 1981): (1) a major event called B1 at 685±15 Ma (Clauer 1976), associated with a regional N90° to N120°E schistosity (S1), greenschist to amphibolite grade metamorphism, and coeval ductile, sinistral E–W shearing, and (2) a second, minor event (B2) at 623±18 Ma (Clauer 1976), which is characterized by E–W upright folds and dextral shearing with axial plane schistosity (S2) and NE–SW faulting. Gasquet et al. (2005) corroborated the general

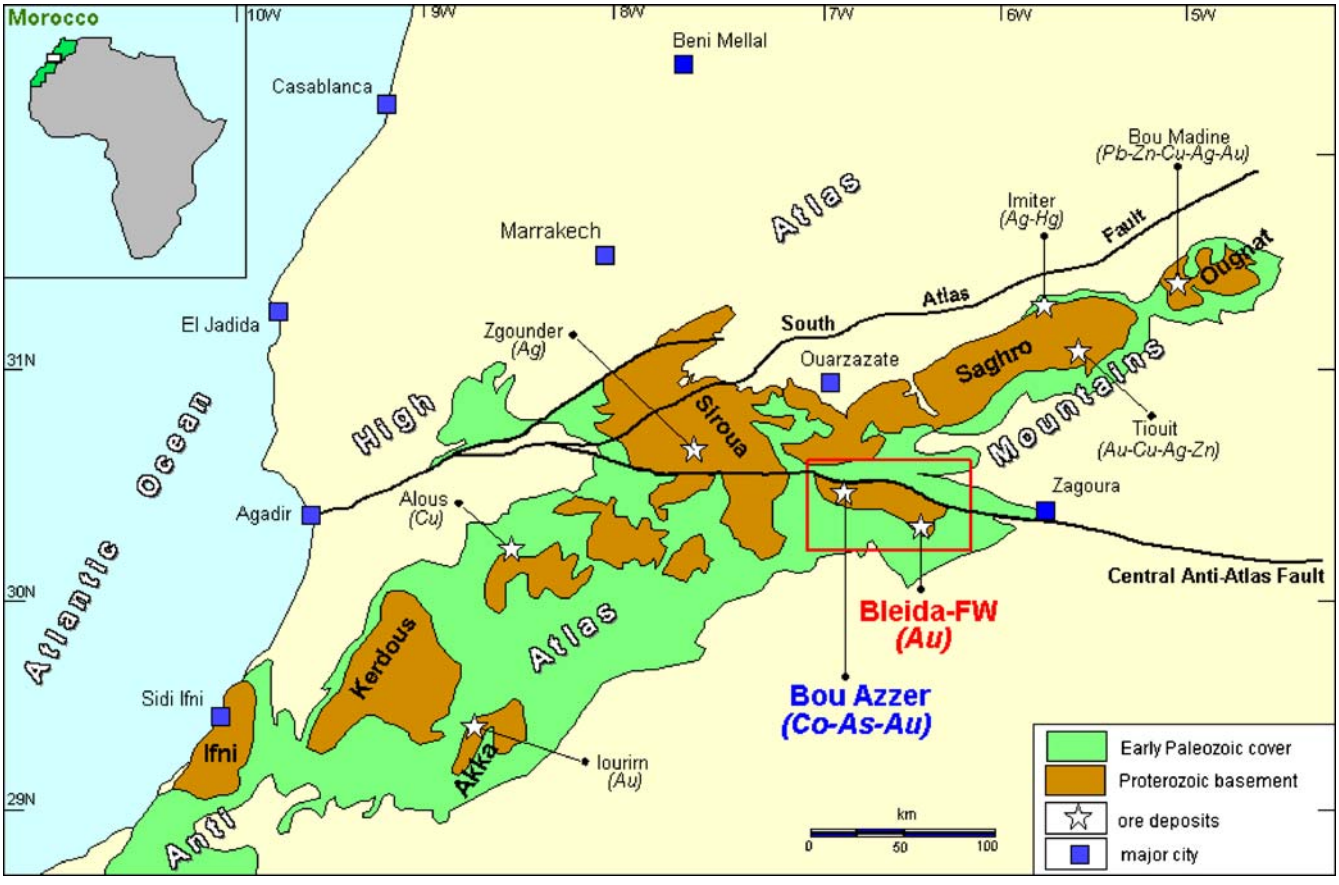

Fig. 1 Major geological units of the Anti-Atlas belt in Morocco, modified after Cheilletz et al. (2002). Also shown are the locations of major noble metal deposits and of the Bleïda Far West deposit

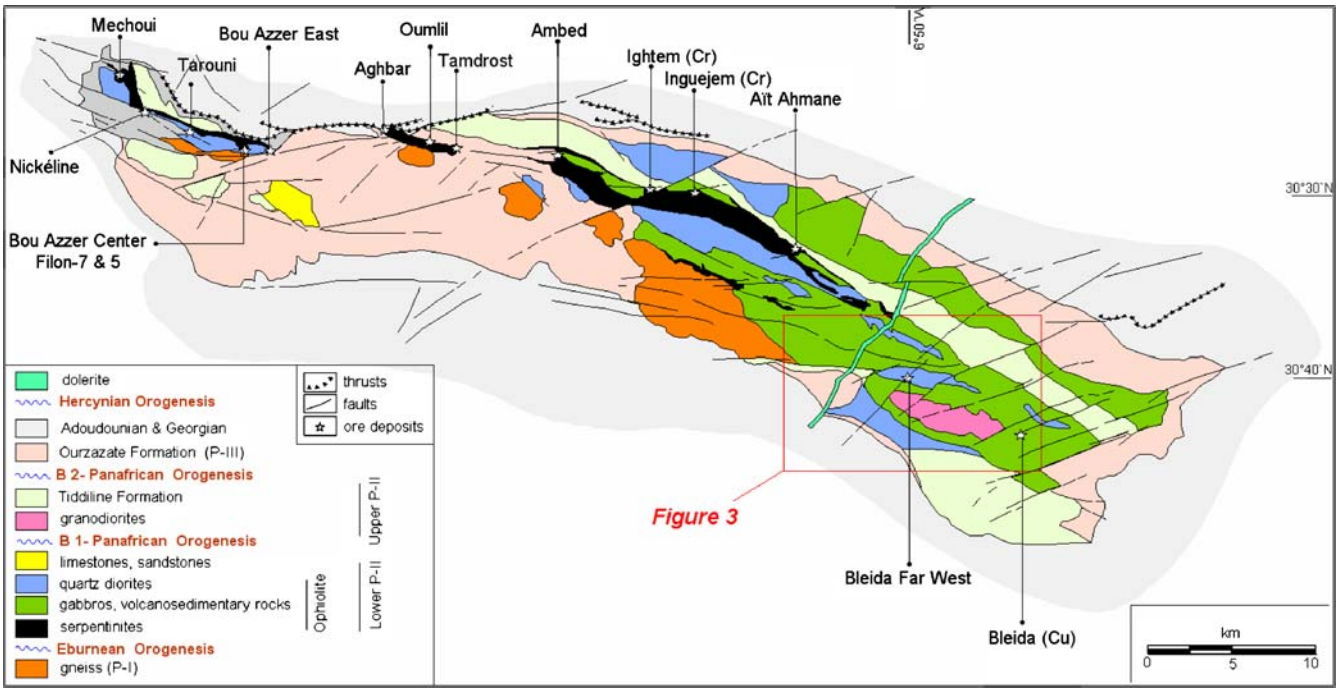

Fig. 2 Geological map of the Bou Azzer–El Graara inlier, modified after Leblanc (1981). Ore deposits of Co–As, chromite (Cr), and copper (Cu) are named and shown by *stars*. The Bleïda Far West area and surroundings shown in Fig. 3 is indicated. Note that the traditional PI to PIII subdivision is also shown in the legend; in the Bou Azzer–El Graara inlier, PI is Paleoproterozoic, PII is Lower and Middle Neoproterozoic, and PIII is Upper Proterozoic (see Thomas et al. 2004 and Gasquet et al. 2005)

significance of these two Pan-African tectonic events at 690–660 and 605 Ma, respectively, also for larger parts of the Anti-Atlas.

In the Bleïda Far West area (Fig. 3), an interlayered series of amphibolites, basic and felsic tuffs, chlorite schists, sericite schists, and cordierite schists of sedimentary and volcanic origin, and quartz diorites are exposed. The intrusive Bleïda granodiorite was recently dated at 579.4±1.2 Ma (Inglis et al. 2004). Metamorphism in the area is generally of greenschist facies (actinolite, albite, epidote/clinozoisite, and chlorite); however, local amphibolite facies of metamorphic grade (hornblende, epidote, calcic plagioclase) has been recorded.

Structures and mineralization

At Bleïda Far West (Fig. 3), gold mineralization is present in a 5×3-km wide corridor consisting of hydrothermally altered amphibolites and chlorite schists. Two structurally controlled, hydrothermal events are distinguished. (1) Early quartz veining related to B1 structures (N 90°–120°) is usually unmineralized, and (2) intense silicification and numerous narrow, variably deformed, and recrystallized quartz-dominated, carbonate- and hematite-bearing veins and breccia zones carry the main gold mineralization and are parallel to the penetrative S2 foliation (N 45°–60°). The ore lodes usually occupy structurally favorable S2 sites in folded, mylonitic bands. The mineralized veins crosscut S1 structures and are synchronous with, or later than, the B2 event. Individual veins are generally narrow (1–2 cm, locally up to 0.5 m wide) and discontinuous along strike and down dip. Three major ore zones extending to depths of at least 100 m have been discovered so far (Fig. 3): (1) the *zone de brèche* (ZB), (2) the *zone centrale* (ZC), and (3) the *zone intermediaire* (ZI). A vertical section of the gold mineralization, showing steep north-dipping, irregular orebodies, and gold grades in the *zone de brèche*, is shown in Fig. 4. Drilling is still in progress to evaluate the geometry of the orebodies and the size of the deposit.

Materials and methods

Samples from drill core (up to 103 m depth) and from the surface were analyzed by inductively coupled plasma mass spectrometry and NiS fire assay-INAA by Actlabs, Canada. At the BGR, light and scanning electron microscopy (SEM), whole rock XRF, and electron microprobe analysis of selected minerals were performed. Gold and platinum group minerals (PGM) grains were analyzed using a CAMECA SX100 electron microprobe operated at the following analytical conditions: accelerating voltage 20 kV, specimen current 30 nA, and measurement times 10 or 20 s. The following X-ray lines and standards were used: Os Mα, Ir Lα, Pt Lα, Au Lα, Ru Lα, Rh Lα, Pd Lα/Lβ, Ag Lβ, Fe Kα, Co Kα, Ni Kα, Cu Kα, Se Lα, Te Lα, Bi Mα, Sn Lα, and Sb Lα (metals), Pd Lα/Lβ (synthetic PdS), S Kα (synthetic $Pt_{0.7}Pd_{0.3}S$, PdS, and pyrite), As Lα (synthetic GaAs). Raw data were corrected using the PAP program supplied by CAMECA. Oxygen was analyzed at

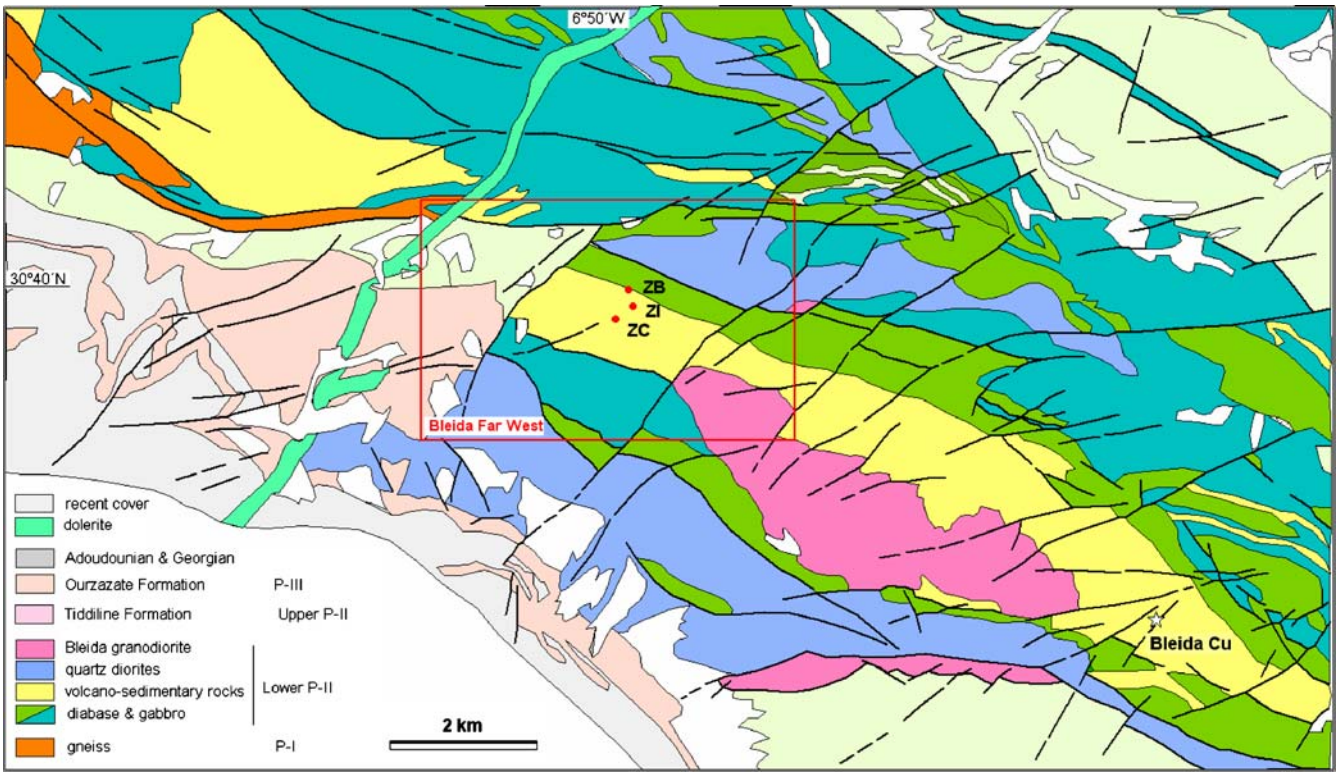

Fig. 3 Simplified geological map of the Bleïda domain of the Bou Azzer–El Graara inlier, modified after Leblanc (1981). Location of the Bleïda Far West gold mineralization and the major ore zones (*ZB = zone de brèche*, *ZC = zone centrale*, *ZI = zone intermediaire*) are indicated

10 kV, 20 nA using a multilayer crystal (PC2), 10 s counting time on peak, a background offset of 1800, and magnetite as standard. Additional corrections were performed for enhancement of the elements Rh, Pd, Ag, Cu, As, and Sb by secondary lines. Detection limits of the analyzed elements are in the order of 0.1 wt%.

Carbonates and quartz were extracted from the ore samples under a binocular microscope by hand and were analyzed for $\delta^{13}C$ and $\delta^{18}O$ by Dr. Tichimova of the stable isotope laboratory of the Technical University of Freiberg. Analyses given are relative to V-PDB (carbon) and V-SMOW (oxygen). The carbon isotopic composition of carbonates was determined using a Finnigan Delta E mass spectrometer following the acid bath procedure of McCrea (1950). Samples were treated with phosphoric acid to form CO_2 gas. Oxygen isotope analyses of quartz were carried out by fluorination with ClF_3 following the method by Borthwick and Harmon (1982). The accuracy of the determinations is better than ±0.2‰.

Fluid inclusions hosted in quartz and calcite were measured using a USGS heating–freezing system by Fluid Inc. with an Olympus BX50 microscope. The stage was calibrated with synthetic inclusions supplied by Synflinc. Gas-bearing inclusions were analyzed with a Jobin-Yvon (formerly Dilor) Raman spectrometer. The exiting radiation used was a 532-nm Nd/Yag laser.

Results

Whole rock geochemistry

In the set of combined drill core and surface samples, gold shows positive correlations with Ag, Pd, and Pt only. Maximum noble metal contents of the investigated ore samples (n=45) are 169.9 ppm Au, 17.8 ppm Ag, 5.57 ppm Pd, and 177 ppb Pt. Au/Ag ratios in deep-seated samples (>50 m depth) vary between 5 and 10 and show a somewhat erratic tendency of increase toward the surface. Overall, the following ratios were obtained from the analyses of the 45 samples: Au/Ag=11.5, Au/Pd=190, and Pd/Pt=16.5.

Sulfur contents are generally below 0.01 wt% (100 ppm) and are accompanied by low-base metal tenors. Maximum contents of Pb are 22 ppm, Cu is usually below 30 ppm but may reach up to 490 ppm in some deep-seated samples, and the maximum contents of Co, Ni, and Zn are 52, 221, and 135 ppm, respectively. Sb, Bi, Te, and As occasionally attain elevated levels of up to 2.1, 19.5, 32.2, and 40.2 ppm, respectively. All mineralized samples notably have distinct contents of manganese (0.2–0.3 wt% Mn).

Ore mineralogy

Gold grains are often visible (millimeter-sized) in drill core samples from greater depth and on fracture planes of

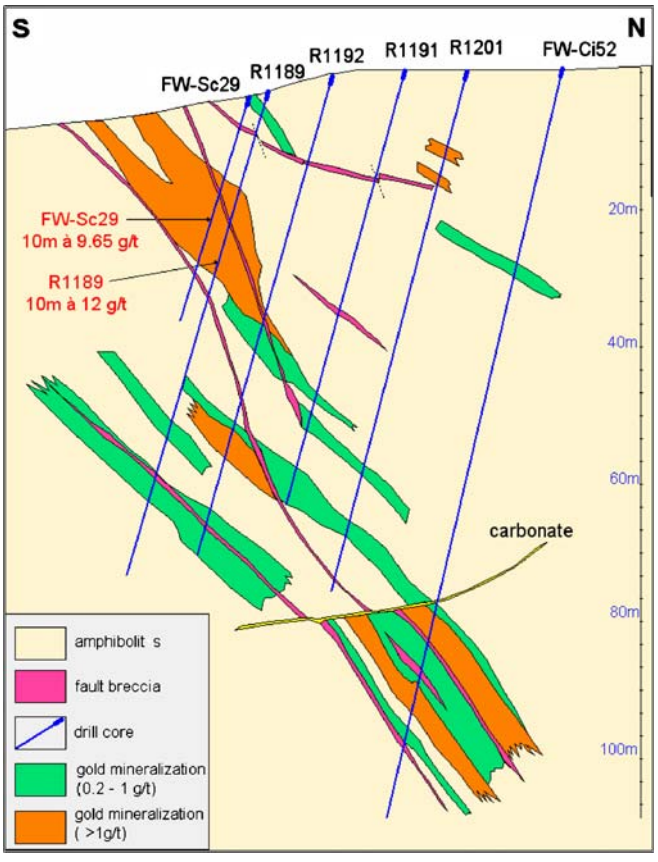

Fig. 4 Vertical section of gold mineralization, location *zone de brèche* (*ZB*). Note steeply north-dipping, irregular orebodies; the term "amphibolites" represents dense volcano-sedimentary rocks

surface samples. Gold is generally interstitial to networks of blades and needles of hematite and is furthermore associated with barite, calcite, and quartz (Figs. 5a–d and 6a,b). The pristine gold–palladium mineralization is virtually sulfide-free; only some rare grains of chalcocite and some very rare grains of a Ag–Bi–Te mineral, probably volynskite ($AgBiTe_2$), and clausthalite (PbSe), were detected (Fig. 6d). The gold grains are often intergrown with a distinct suite of platinum group minerals (PGM; see below). In some deep-seated samples (70–103 m), a disseminated, brecciated sulfide assemblage consisting of rare chalcocite, covellite, chalcopyrite, pyrite, and bornite occurs in a ferruginous breccia matrix and in vein quartz fragments. However, this Cu-rich mineralization is not associated with gold and may, therefore, belong to a different mineralizing event.

Visible gold grains associated with iron oxides and iron hydroxides, Mn–Fe, and Mn–Bi–V oxides are frequently present on fractures of surface samples. The presence of large gold grains (up to 3 mm in diameter) probably indicates redistribution of the noble metal in the exogenic environment.

Gold

In polished sections, gold grains with sizes up to 300 μm are in association with specular hematite and variable amounts of quartz, calcite, barite, epidote, and chlorite (Figs. 5a–d and 6a,b,h). Gold occurs as open-space filling in fragments of hematite-rich material and intergrown with specular hematite, calcite, and quartz. Gold is usually optically homogeneous; however, it locally contains inclusions of a suite of PGM or is intergrown with PGM grains along its peripheries (e.g., Fig. 6f,g).

The composition of gold (Table 1) ranges from 79 to 93 wt% Au, 6 to 19 wt% Ag, and 0.5 to 6.29 wt% Pd. Mercury contents are generally close to the detection limit of the method (ca. 0.1 wt% Hg); however, in rare instances gold grains contain up to 1.33 wt% Hg. Copper concentrations in the range 0.2 to 1.0 wt% Cu (average 0.54, maximum 3.13 wt% Cu) are constantly present. Notably, one 8-μm large, free grain of tetraauricupride (AuCu) was also detected (Table 1).

The histograms (Fig. 7a,b) show a grossly unimodal distribution of Ag in gold (average silver content is 8.62 wt% Ag; n=123 analyses). Differences between the different ore zones are regarded insignificant. No distinct trend of pervasive supergene leaching of silver from the gold grains can be distinguished, although it was observed in some instances that gold grains are rimmed or cut by veinlets (up to about 10 μm wide) of pure gold at their margins, exemplified by a number of analyses between 0–4 wt% Ag (Fig. 7a). Equally, the histogram of Pd contents of gold (Fig. 7b) indicate a persistent, even (unimodal?) distribution of Pd in gold (average Pd content is 0.50 wt% Pd; n=123).

Platinum group minerals

The following mineral names and formulae of the PGM are kept in accordance with the proposals given by Cabri (2002). All grains of PGM observed are either included in gold or intergrown with gold. In decreasing order of abundance, mertieite-I or isomertieite, both ($Pd_{11}Sb_2As_2$), keithconnite ($Pd_{3-x}Te$), and a Bi-rich variant of keithconnite [~$Pd_{20}(Te,Bi)_7$], palladseite ($Pd_{17}Se_{15}$), merenskyite ($PdTe_2$), merenskyite–moncheite [$(Pd,Pt)(Te,Bi)_2$], kotulskite (PdTe), and sperrylite ($PtAs_2$) were identified in the ores. Their grain sizes range from about 5 to 40 μm.

Microprobe analyses (Table 2) show the following peculiarities of the PGM.

Mertieite-I or *isomertieite*, both ($Pd_{11}Sb_2As_2$), are treated together, as according to Cabri (2002), isomertieite (cubic) and mertieite-I (hexagonal) are hard to distinguish optically (light yellowish white to brass or cream-yellow; anisotropy indistinct), both have Sb/As ratios near unity, and usually have low contents of other elements besides Pd, As, and Sb. Typical intergrowths are shown in Figs. 5e–h and 6b,c,e,f.

Mertieite-I/isomertieite from Bleïda Far West is characterized by a constant chemical composition. The average

formula calculated from 35 analyses is ($Pd_{10.9}Sb_{1.97}As_{1.84}$). Sb/As ratios range from 1.02 to 1.21 (average 1.07). Analyses of isomertieite reported in Cabri (2002) all have Sb/As <1, whereas those of mertieite-I have Sb/As ≥1. The following elements were detected in minor to trace amounts: Fe (up to 8.7 at.%), Cu (up to 3.1 at.%), Se (up to 0.12 at.%), Sn (up to 0.15 at.%), Te (up to 0.20 at.%), Bi (up to 0.11 at.%), and Pt (up to 0.17 at.%).

Keithconnite ($Pd_{3-x}Te$) is second in abundance after isomertieite/mertieite-I. Typical intergrowths are shown in Figs. 5h and 6f. Keithconnite carries traces of Fe (up to 2.6 at.%), Cu (up to 1.8 at.%), As (up to 0.3 at.%), Se (up to 0.2 at.%), Ir (up to 0.5 at.%), Pt (up to 1.4 at.%), and Hg (up

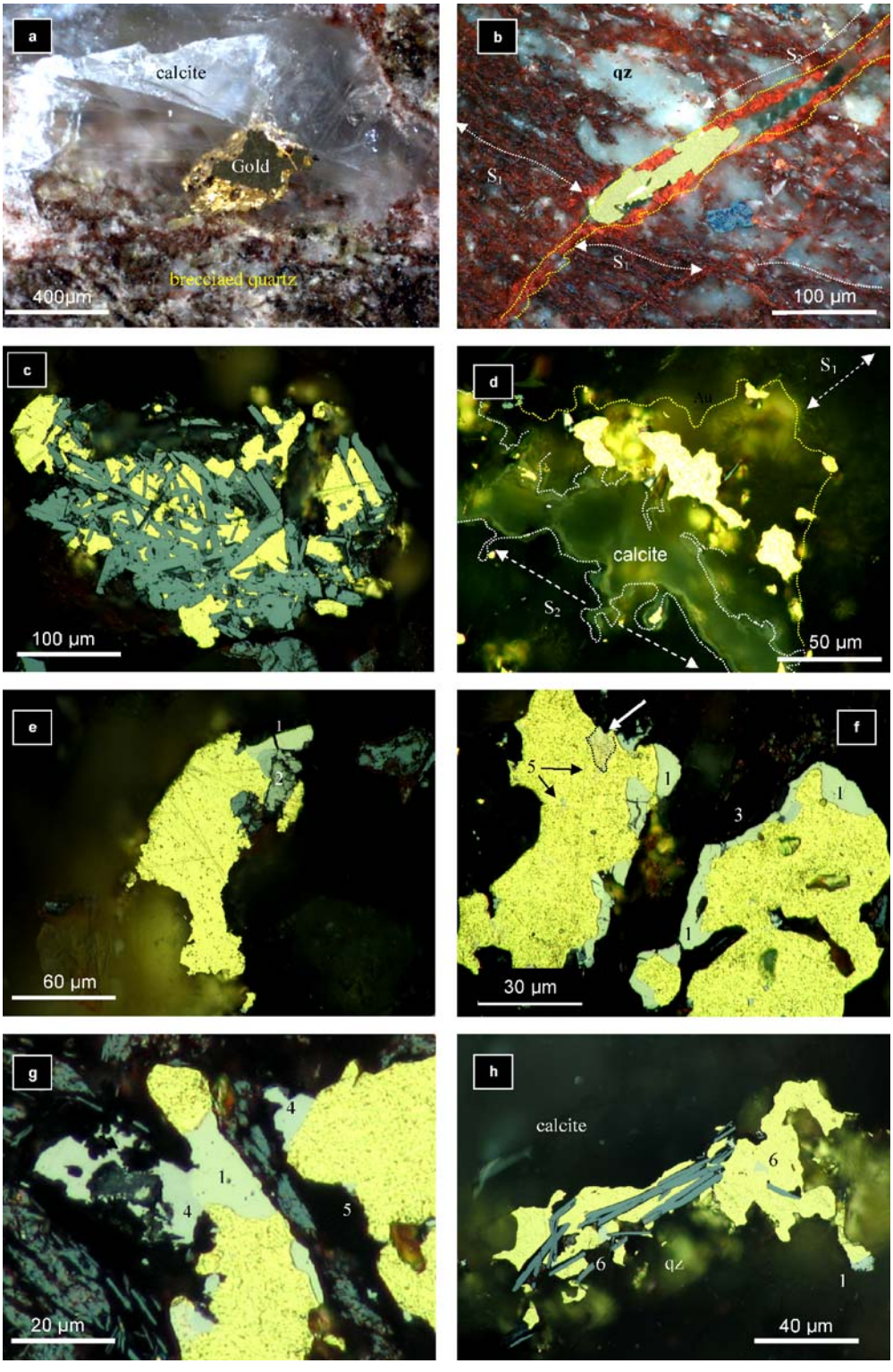

Fig. 5 Photomicrographs (**a** binocular microscope, **b**–**h** reflected light microscope images taken in oil immersion). PGM shown are *1* mertieite-I/isomertieite, *2* palladseite, *3* kotulskite, *4* merenskyite, *5* sperrylite, *6* keithconnite. **a** Larger gold grain enclosed in calcite. AS 7007b, ZB-24m. **b** Calcite veinlet parallel S2 with fine-grained hematite (*red*) along the contacts and hosting gold (*yellow*). AS 7169, ZB-18.6m. **c** Larger aggregate of gold (*yellow*) intergrown with laths of hematite (*mediumgray*). Small PGM grains are attached to and included in gold (only faintly visible). AS 6830a, ZB-40m. **d** Gold in calcite vein parallel S2 (crosscutting S1). AS 6830a, ZB-40m. **e** Gold grain with attached mertieite-I/isomertieite (*1*) and palladseite (*2*). AS 6830a, ZB-40m. **f** Kotulskite (*3*), tiny grains of sperrylite (*5*), and mertieite-I/isomertieite (*1*) intergrown with gold (ca. 8 wt% Ag), which has silver-poor (<0.5 wt% Ag) areas (*arrow*). AS 7175a, ZB-23.8m. **g** Gold, merenskyite (*4*), sperrylite (*5*), and mertieite-I/isomertieite (*1*). AS 7175a, ZB-23.8m. **h** Gold grain intergrown with laths of hematite (*mediumgray*) and keithconnite (*6*). Gangue (*black*, internal reflections) is calcite and quartz. AS 7169, ZC-16.4m

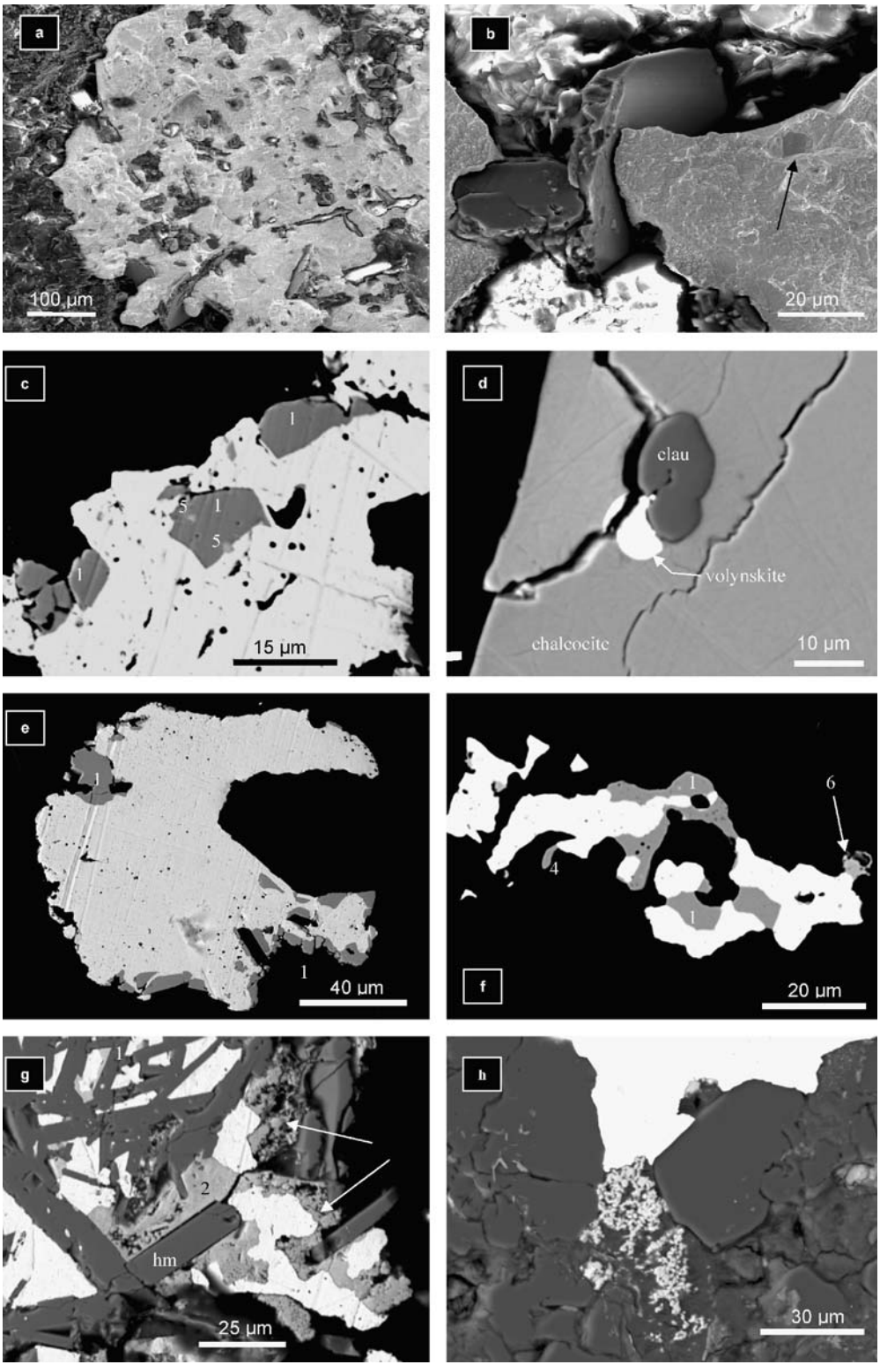

Fig. 6 Scanning electron microscope (SEM) images (**a** and **b**) and backscatter electron images (**c**–**h**) of gold and PGM. **a** Large gold grain (*mediumgray*) transected by laths of hematite (*darkergray*). *Zone de brecche* (*ZB*), surface sample FW-04-08. **b** Intergrowth of gold (*mediumgray*), hematite (*darkgray*), and barite (*white*). Note small grain of mertieite-I/isomertieite (*arrow*). *Zone de brecche* (*ZB*), surface sample FW-04-08. **c** Gold (*white*) intergrown with mertieite-I/isomertieite (*1*) and sperrylite (*5*). AS 6830, ZB-40m. **d** Volynskite (AgBiTe2; *white*), and clausthalite (PbSe; *darkergray*) included in chalcocite (*mediumgray*). AS 7023, ZB-67m. **e** Mertieite-I/isomertieite (*1*, *darkergray*) intergrown with gold (*lightgray*). AS 6830, ZB-40m. **f** Gold intergrown with mertieite-I/isomertieite (*1*), merenskyite (*4*), and keithconnite (*6*). AS 7175a, ZB-23.8m. **g** Gold (*white*) embedded in network of hematite laths (*darkestgray*). *Mediumgray* includes mertieite-I/isomertieite and palladseite (*2*), as well as porous secondary Pd-oxides/hydroxides (*arrows*). AS 6830a, ZB-40m. **h**. Porous, secondary Pd-oxides/hydroxides (*mediumgray*) surrounded by Mn-oxides and carbonate (*darkestgray* to *black*) hard to distinguish, in contact with gold grain (*white*). AS 7007c, ZB-24m

to 2.4 at.%). The concentrations of Bi may reach 6.4 at.% or 11.6 wt%. This is considerably higher than the maximum value of 3.4 wt% reported in Cabri (2002). In fact, Te and Bi form a solid solution up to 19 at.% Te and 6 at.% Bi (Fig. 8), or 0.75 apfu Te and 0.25 apfu Bi, calculated on the basis of four atoms. A group of ten analysis points at the Bi-rich end may indicate that an intermediate member with Bi/(Bi+Te)=0.25 exists in the $Pd_3(Te,Bi)$ system. This ternary phase was not observed in experiments carried out at 489°C (see Makovicky 2002), and thus probably forms at lower temperature.

Palladseite ($Pd_{17}Se_{15}$) was found in one sample only (Fig. 5e). As an average of six analyses, palladseite contains 52.8 at.% Pd, 40 at.% Se, 2.8 at.% Cu, 2.0 at.% Bi,

Table 1 Representative microprobe analyses of gold and tetra-auricupride

Sample/analysis	Gold 6830/37	Gold 7016/7	Gold 7019/4	Gold 7022/2	Gold 7023/10	Gold 7169/14	Gold 7175a/11	Gold 7184/5	Tetra-auricupride 7176b/14
Locality/zone	Breches	Central	Breches N–S	Breches E–W	Breches E–W	Central	Breches N–S	Central	Interméd.
Drill core	Ci-49	ZC-1	R1114	Sci-52	Sci-52	FWB-Sc24	FWB-Sc28	FWB-Sc38	FWB-Sc29
Depth (m)	60–70	Trench	32–33	60–61	67–68	16.5	23.8	23.9	12.9
S	0.04	0.02	0.10	0.08	0.09	bdl	0.05	0.03	0.03
Cu	0.80	0.68	0.25	bdl	3.09	1.39	bdl	bdl	21.54
Pd	0.88	0.90	bdl	6.29	bdl	0.91	3.24	0.04	0.22
Ag	7.06	4.54	11.94	1.47	19.74	2.75	2.59	0.67	0.09
Au	91.11	94.43	87.81	91.44	78.74	94.56	94.27	98.48	78.37
Hg	bdl	bdl	bdl	bdl	1.26	bdl	bdl	bdl	bdl
Total (wt%)	99.89	100.56	100.10	99.43	102.92	99.67	100.20	99.22	100.25
Atomic percent									
S	0.21	0.10	0.53	0.45	0.41		0.29	0.20	0.11
Cu	2.30	1.97	0.71		7.60	4.09			45.78
Pd	1.50	1.56	0.00	10.96		1.59	5.69	0.07	0.28
Ag	11.90	7.78	19.64	2.52	28.58	4.75	4.49	1.22	0.11
Au	84.09	88.59	79.12	86.06	62.43	89.57	89.53	98.51	53.72
Hg					0.98				

Selected microprobe analyses showing the range of gold compositions, and tetra-auricupride of the Bleïda Far West gold mineralization
Detection limits: 0.02% (S), 0.04% (Cu, Pd), 0.08% (Ag), 0.35% (Hg)
bdl Below the limit of detection

and minor Fe (up to 0.9 at.%), Te (up to 0.2 at.%), Hg (up to 0.2 at.%), and V (up to 0.6 at.%). The obtained average formula is $[(Pd_{16.9}Cu_{0.9})_{17.8}(Se_{12.8}Bi_{0.7})_{13.5}]$, consequently deviating from the stoichiometric 17/15 ratio. Olivo and Gauthier (1995) and Cabral et al. (2002c) also reported deviating Pd/Se ratios (19/13 and 18/14, respectively) of palladseite from the Cauê mine, Minas Gerais, Brazil.

Merenskyite ($PdTe_2$) was found in two samples only (Figs. 5g and 6f). Minor elements detected in five analyses include Pt (up to 1.9 at.%) and Bi (up to 1.4 at.%). The average formula is $[(Pd_{0.98}Pt_{0.03})_{1.01}(Te_{1.93}Bi_{0.04})_{1.97}]$. In addition, one grain of merenskyite–moncheite solid solution was found, corresponding to $[(Pd_{0.83}Pt_{0.17})_{1.0}(Te_{1.86}Bi_{0.12})_{1.98}]$.

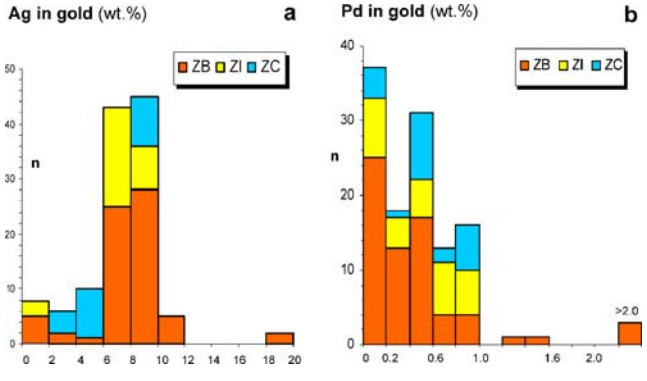

Fig. 7 Histograms of gold compositions analyzed by microprobe. **a** Silver contents of gold (wt%), **b** Palladium contents of gold (wt%). *ZB = zone de brèche*, *ZC = zone centrale*, *ZI = zone intermediaire* at Bleïda Far West

Kotulskite (PdTe) is a rare mineral at Bleïda Far West (Fig. 5f). Its composition corresponds to $[Pd(Te_{0.79}Bi_{0.21})]$, thus having a considerable miscibility toward sobolevskite (PdBi). Pt and Sb concentrations are below the detection limit of the microprobe.

Sperrylite ($PtAs_2$) is present as tiny (<5 μm) inclusions in isomertieite/mertieite-I or in gold in several samples (Figs. 5f,g and 6c). Most of the grains are too small for quantitative analysis. Three measured grains do not differ substantially from the stoichiometric composition, averaging $[(Pt_{0.94}Fe_{0.02}Cu_{0.01})_{0.97}(As_{1.85}Se_{0.04}S_{0.06}Te_{0.06})_{2.01}]$.

Potarite (PdHg). One tiny grain (~3 μm in diameter) was found carrying considerable Hg contents in addition to Pd, and some S, Te, Cu, and Fe. This grain may be potarite (PdHg); however, Daltry and Wilson (1997) listed several other unnamed Pd–Hg (Te–Bi–Ag) compounds.

Secondary PGM are regarded as products of exogenic weathering and mainly consist of ill-defined phases or mixtures of oxides or hydroxides containing the elements Pd, Bi, Te, Se, V, Cu, Fe, and Mn (Fig. 6g,f). Mertieite-I and palladseite are locally replaced by a Pd-rich oxide/hydroxide phase (Fig. 6g). Two distinct groups of "oxides" may be distinguished (see Table 3 and Fig. 9):

Group 1

Dominated by Bi (>50 wt%) and about 10 wt% Pd, 15 wt% V, some Se (up to 2.4 wt%), and traces of Fe, Cu, Te, Pb, and Mn. Oxygen concentrations, measured in a few grains, range from 10 to 13 wt%.

Table 2 Microprobe analyses pertaining to platinum-group minerals, first expressed in wt%, then in atoms per formula unit with the sums shown in the last column (Z)

Sample	Analysis	Location	Mineral	Pd	Pt	Sb	As	Te	Bi	Hg	S	Se	V	Mn	Fe	Cu	Total
6830-12a	27	ZB-40m	Mertieite-I*	75.01	0.03	15.21	9.15	0.19	0.10		0.02		0.02		0.41	0.13	100.27
7175a-7e	22	ZB-23m	Mertieite-I*	73.64		15.51	8.74	0.03			0.02		0.03	0.02	0.43	0.33	98.75
7176b-15b	3	ZI-12.9m	Mertieite-I*	74.01		15.46	8.79	0.18	0.04						0.16	0.30	98.94
7021-1d	1	ZB-13m	Merenskyite	28.40	1.51			68.84	2.44		0.02	0.02		0.02		0.03	101.27
7007c-2a	6	ZB-24m	Kotulskite	42.24	0.04			39.82	17.90			0.03			0.02		100.06
7012a-2b	3	ZI-44m	Keithconnite	68.49	1.17			27.26	3.06		0.04	0.06			0.57	0.03	100.67
7175a-7e	21	ZB-23m	Keithconnite-(Bi)	67.81	0.01		0.15	21.64	11.03		0.02				0.18		100.84
7007c-2c	10	ZB-24m	Keithconnite-(Bi)	69.02	0.13		0.05	22.73	10.00	0.24		0.03			0.03	0.06	102.28
6830-14b	34	ZB-40m	Palladseite	58.30	0.18			0.41	5.61	0.16		31.16	0.44	0.13	0.81	1.67	98.87
6830-2c	7	ZB-40m	Palladseite	56.15	0.10			0.10	3.20	0.72	0.04	34.90	0.02		0.11	1.61	96.96
6830-13d	32	ZB-40m	Sperrylite		47.05		34.39	1.52	0.07		0.47	1.00	0.02		0.09	0.05	84.66
				Pd	Pt	Sb	As	Te	Bi	Hg	S	Se	V	Mn	Fe	Cu	Z
6830-12a	27	ZB-40m	Mertieite-I*	10.95	0.00	1.94	1.90	0.02	0.01		0.01		0.01		0.11	0.03	15
7175a-7e	22	ZB-23m	Mertieite-I*	10.91		2.01	1.84	0.00			0.01		0.01	0.00	0.12	0.08	15
7176b-15b	3	ZI-12.9m	Mertieite-I*	10.97		2.00	1.85	0.02	0.00						0.05	0.07	15
7021-1d	1	ZB-13m	Merenskyite	0.97	0.03			1.95	0.04		0.00	0.00		0.00		0.00	3
7007c-2a	6	ZB-24m	Kotulskite	1.00	0.00			0.78	0.22			0.00			0.00		2
7012a-2b	3	ZI-44m	Keithconnite	2.89	0.03			0.96	0.07		0.01	0.00			0.05	0.00	4
7175a-7e	21	ZB-23m	Keithconnite-(Bi)	2.93	0.00		0.01	0.78	0.24		0.00				0.01		4
7007c-2c	10	ZB-24m	Keithconnite-(Bi)	2.95	0.00			0.81	0.22	0.01		0.00			0.00	0.00	4
6830-14b	34	ZB-40m	Palladseite	17.10	0.03			0.10	0.84	0.00		12.32	0.27	0.07	0.45	0.82	32
6830-2c	7	ZB-40m	Palladseite	16.56	0.02		0.00	0.02	0.48	0.11	0.04	13.87	0.01		0.06	0.80	32
6830-13d	32	ZB-40m	Sperrylite	0.00	0.97		1.85	0.05	0.00		0.06	0.05	0.00		0.01	0.00	3

Rh, Ru, Os, Ir, Pb, Sn, Si, and free fields are below the detection limit. Low totals in some analyses are due to the contribution of (Au,Ag) host minerals, which were subtracted for all analyses
*Mertieite-I** Mertieite-I/isomertieite (see text)

Group 2

Dominated by Pd (64–83 wt%) and variable amounts of Bi, Cu, Se, Te, Fe, Mn (up to 2.3 wt%), and V (up to 2.6 wt%). A more Bi-rich subgroup (11–13 wt% Bi) contains 5.8 to 11.3 wt% O and up to 6.4 wt% Se besides distinct V, Fe, Mn, Cu, and Te contents. A more Cu-rich subgroup (1.7–6.8 wt% Cu) carries less Bi (up to 5.6 wt%) and 1.5–4.3 wt% O. Metal/oxygen ratios on an atomic basis are close to 1 for group 1, and >1 to 6 for group 2.

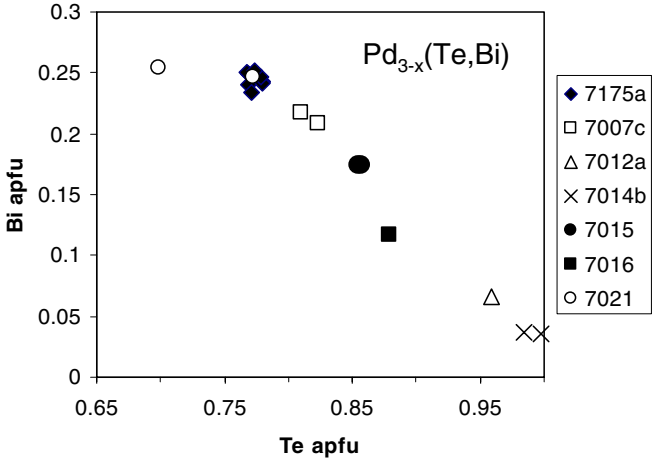

Fig. 8 Chemical composition of keithconnite from Bleïda Far West. Apparent solid solution of keithconnite and a hypothetical Bi end member in a Te–Bi diagram. *apfu* Atoms per four atoms in formula unit. *Symbols* denote different samples

Bi–Pd oxides similar to group 1 have been described from Chiney, Aldan Shield (Tolstykh et al. 2000); oxygen concentrations range from 6.5 to 12.5 wt%, Pd from 7 to 24 wt%, and Bi from 67 to 85 wt%. However, V was not reported in these analyses. The Pd-rich oxides of group 2 closely resemble alteration products of Pd–bismuthotellurides reported from the Great Dyke, Zimbabwe (Oberthür and Melcher 2005; Locmelis 2005).

In summary, the gold mineralization at Bleïda Far West is characterized by negligible sulfide contents and the association of gold with predominant hematite and barite. Calcite and quartz are the main gangue minerals accompanying the mineralization. The particulate gold is silver- and palladium-bearing and shows intergrowths with grains of a number of PGM, all Pd compounds with metalloids like Sb, As, Te, Bi, and Se. Sperrylite and merenskyite–moncheite are the only rarely observed platinum-dominated PGM.

Table 3 Microprobe analyses of secondary platinum-group element compounds (Pd-oxides/hydroxides) of the Bleïda Far West gold mineralization

Sample	Analysis	Location	Mineral	Pd	Pt	Au	Bi	Ag	Te	Hg	V	Mn	Fe	Cu	Se	S	Si	O	Total
6830-5c	17	ZB-40m	Pd-Bi-O	67.62	0.20		12.87		0.08		1.44	1.53	2.13	1.03	0.10	0.04	0.07	n.a.	87.12
7175a-13a	31	ZB-23m	Pd-Bi-O	79.25	0.04	0.80	3.01	0.08	1.07		0.60	0.84	1.43	1.36		0.22	0.38	n.a.	89.09
7007c-2a	7	ZB-24m	Pd-Cu-Bi-O	78.73	0.23	0.95	2.26	0.05	0.89	0.20	0.47	0.45	0.64	4.80		0.12	0.11	4.09	93.99
7021-4c	4	ZB-13m	Pd-Bi-Te-O	64.19	0.06	0.80	13.10	0.08	5.46	0.08	0.88	1.96	0.99	0.26	0.04	0.07	0.33	9.21	97.52
6830-5d	11	ZB-40m	Bi-Pd-V-O	12.84	0.00	1.33	53.35	0.65	0.06	0.24	12.48	0.14	0.83	0.21	2.35	0.06	0.05	10.66	95.26
6830-14b	35	ZB-40m	Bi-Pd-V-O	7.58	0.00	1.33	56.59	0.76	0.09		14.19	0.13	0.44	0.14	1.69	0.02		12.13	95.09

Rh, Ru, Os, Ir, As, Sb, and free fields are below the detection limit
n.a. Not analyzed

Stable isotopes

The limited isotopic data available recommend caution concerning the discussion on the sources and fate of the fluids that deposited quartz and carbonates. The two quartz samples have $\delta^{18}O$ values of 10.4 and 14.1 ‰ (V-SMOW). These values correspond to the range of data (10–16‰) typical for vein quartz from hydrothermal gold deposits of all ages (e.g., Kerrich 1987). The carbon and oxygen isotopic compositions of the calcite samples (n=5) from Bleïda Far West are illustrated in Fig. 10. The values of $\delta^{18}O$ range from 12.8 to 20.7‰ (V-SMOW), and those of $\delta^{13}C$ occupy a tight range from −7.0 to −9.7‰ (V-PDB). The Bleïda Far West carbonate isotope compositions occupy a field distinct by lighter $\delta^{13}C$ values from the carbon and oxygen isotope compositions of carbonates from the Bou Azzer Co–As ores shown for comparison. In general, the $\delta^{18}O$ and $\delta^{13}C$ ranges indicate an origin of the carbonates (and quartz) from metamorphic–magmatic hydrothermal solutions (Barnes 1979, 1997; Kyser 1987; Rollinson 1993) for both the Bleïda Far West and the Bou Azzer ores.

The $\delta^{18}O$ values of the carbonates indicate formation by metamorphogenic solutions. The variability in the $\delta^{18}O$ values attests to compositional variations and physico-chemical changes of the hydrothermal fluid. The large spreads of both mineralizations (about 8‰) may be related to mixture with meteoric fluids or boiling processes (Barnes 1997).

According to Kerrich (1987), carbonate $\delta^{13}C$ values around −5‰ are hard to interpret with regard to the carbon source because magmatic, sedimentary, and metamorphic rocks are all characterized by average $\delta^{13}C$ values in this range. Carbonate carbon isotopic compositions of the samples from Bou Azzer (~ −4‰), from the oceanic domain of the ophiolite, probably show a primary magmatic carbon isotope signature typical for mafic magmas ($\delta^{13}C$~ −5.5‰), indicating reactions of the mineralizing fluid with the serpentinite/diorite wall rocks. The comparably lighter $\delta^{13}C$ values (−7.0 to −9.7‰) at Bleïda Far West, situated in the continental margin domain,

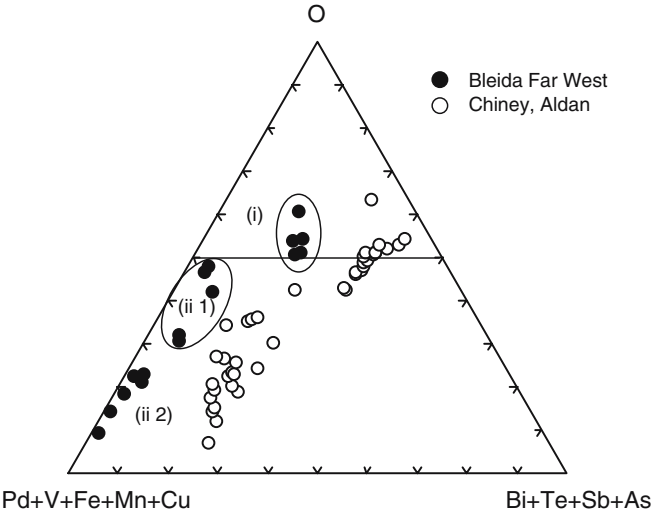

Fig. 9 Chemical composition of oxidized PGM phases from Bleïda Far West. Triangular diagram (at.%) showing the composition of Bi-rich (*i*) and Pd-rich oxides (*ii*), compared with data from Chiney (Tolstykh et al. 2000). Pd–Bi dominated oxides (*ii 1*), Pd–Cu-dominated oxides (*ii 2*). For explanations, see text

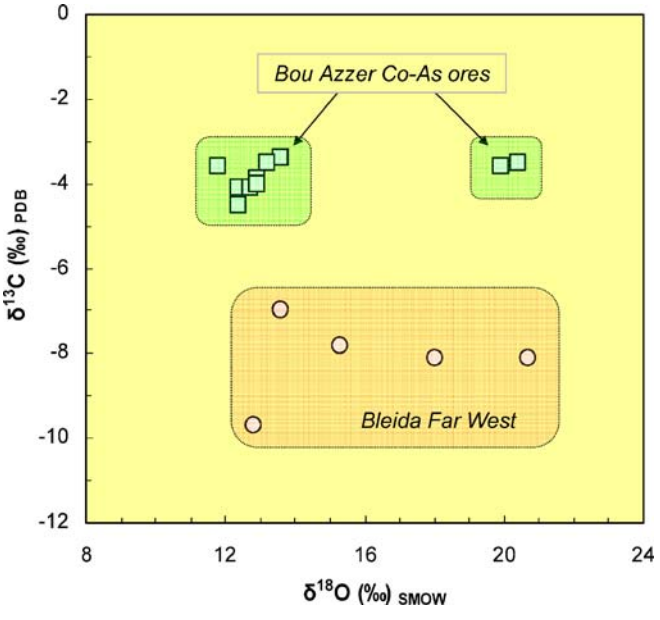

Fig. 10 Plot of oxygen ($\delta^{18}O$) versus carbon ($\delta^{13}C$) stable isotope compositions of calcite from Bleïda Far West. Carbonates from the Bou Azzer Co–As ores are shown for comparison. The separate group ($\delta^{18}O$ values of 19.9 and 20.4) are samples from Agoudal/Tamdrost

indicate isotopic exchange with an organic (graphite) or carbonate carbon reservoir in the sedimentary-volcanic wall rocks. The large spread of about 4‰ likely results from isotope fractionation related to boiling or fluid mixing processes rather than temperature variation, which has little impact on carbon isotope composition in the temperature range between 300 and 150°C (Barnes 1979; Ohmoto and Goldhaber 1997).

Fluid inclusion studies

Barakat et al. (2002) performed fluid inclusion studies in quartz from gold showings of Bleïda Far West and concluded that the formation of quartz occurred by cooling of fluids with highly variable salinity from 300 to 150°C under a decreasing pressure regime (from about 50 MPa to less than 4 MPa at 150°C). Furthermore, the authors pointed to an epithermal setting, probably related to Late Pan-African magmatism. The fluid inclusions studied are hosted in small quartz and calcite veins obtained from core sections of the three exploration areas shown in Fig. 3. Where present in the same fissure, quartz is always older than sparry calcite.

Fluid inclusions in quartz occur in planes and clusters and due to the locally high frequency of fluid inclusions in a single quartz grain, a clear classification in primary vs secondary origin according to Roedder (1984) is often vague or even impossible. However, in general, the same fluid inclusion types are present in the studied samples of quartz as previously described by Barakat et al. (2002). These are (1) carbonic ($\pm N_2$, CH_4) inclusions with highly variable water content (5–70%) and variable sizes and shapes (Fig. 11a), and (2) secondary two-phase aqueous inclusions. The melting temperatures of solid CO_2 in carbonic inclusions were mostly measured around −57°C and fell below the triple point of pure CO_2 (−56.57°C), indicating the presence of other gases besides CO_2 in the inclusions. Laser Raman analyses proved variable amounts of N_2 (1.5 to 2 mol%) and locally up to 1 mol% CH_4 in the carbonic inclusions. Melting of liquid CO_2 into the vapor phase occurred in the temperature range between 25.5 and 30.2°C. The salinity of water-rich carbonic inclusions was determined to be about 6–8 wt% NaCl equivalent via clathrate melting using the methods described by Barton and Chou (1993) and Bakker et al. (1996). Final homogenization temperatures were only obtained from carbonic inclusions with high water content and fall into the temperature range between 280 and 325°C. Carbonic inclusions with water content lower than 50% decrepitated before final homogenization.

Aqueous two-phase fluid inclusions in quartz occur along secondary trails and show a wide range in their final ice melting temperatures and homogenization temperatures (Fig. 12a). Most of the ice melting temperatures lie between −17 and 0°C, which corresponds to salinities from 0 to about 20.4 wt% NaCl equivalent.

Fluid inclusions in calcite A different situation is recorded in fluid inclusions in calcite. Fluid inclusions in calcite that appear to be of primary origin (Roedder 1984) are aqueous two-phase and occasionally host an additional solid phase, which does not dissolve during heating runs (Fig. 11b). The final melting temperatures of ice and clathrate scatter over a broad temperature range between −35 and +1.7°C (Fig. 12b), and two subgroups of fluids may be present. One subgroup overlaps with the fluid inclusion range of quartz (Tm_{ice} down to −18°C), and the other has Tm_{ice} between −15 and −35°C. The homogenization temperatures obtained are highly variable. Most of them vary between 150 and 250°C. For some individual samples, it appears that high-salinity fluid inclusions tend to have lower homogenization temperatures than low-salinity fluid inclusions, probably due to mixing of a colder saline fluid with a low-salinity hydrothermal fluid (Fig. 12b).

The interpretation of the fluid inclusion data is problematic due to the high frequency of differently composed fluid inclusions in quartz and calcite. Nevertheless, it appears that the oldest (probably primary) inclusions in quartz are rich in CO_2 ($\pm CH_4$–N_2) and have variable water contents. Barakat et al. (2002) discriminated between two generations of quartz in their studied sample material. The older quartz hosts primary inclusions where the volatile phase occupies more than 85 vol.% of the total volume of the inclusions. In the younger quartz generation, the volume of the gas phase is lower (45–65 vol.%). Our samples host both types of inclusions suggesting that they represent a second generation of quartz. Furthermore, some of the quartz fissures additionally contain younger calcite in the center of the fissures that is devoid of gas-rich

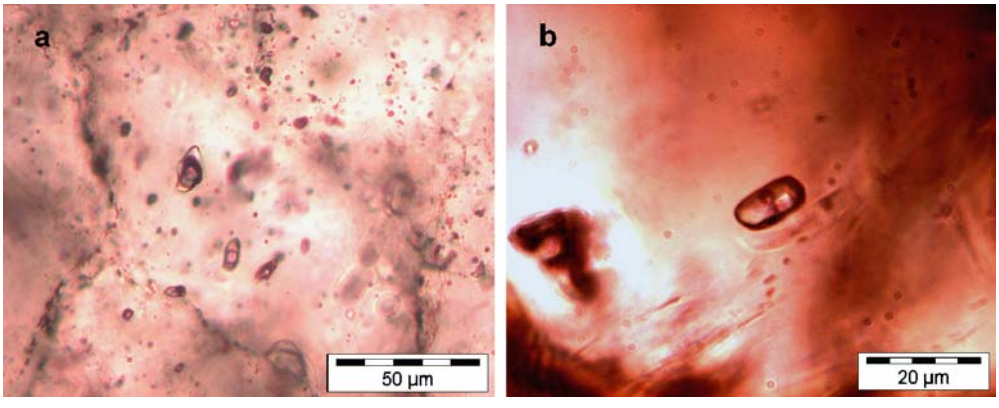

Fig. 11 **a** Cluster of aqueous-carbonic ($\pm CH_4$, N_2) fluid inclusions in quartz (sample FW04-53). **b** Primary fluid inclusion with daughter crystal of halite (?) in calcite (sample FW-04-31)

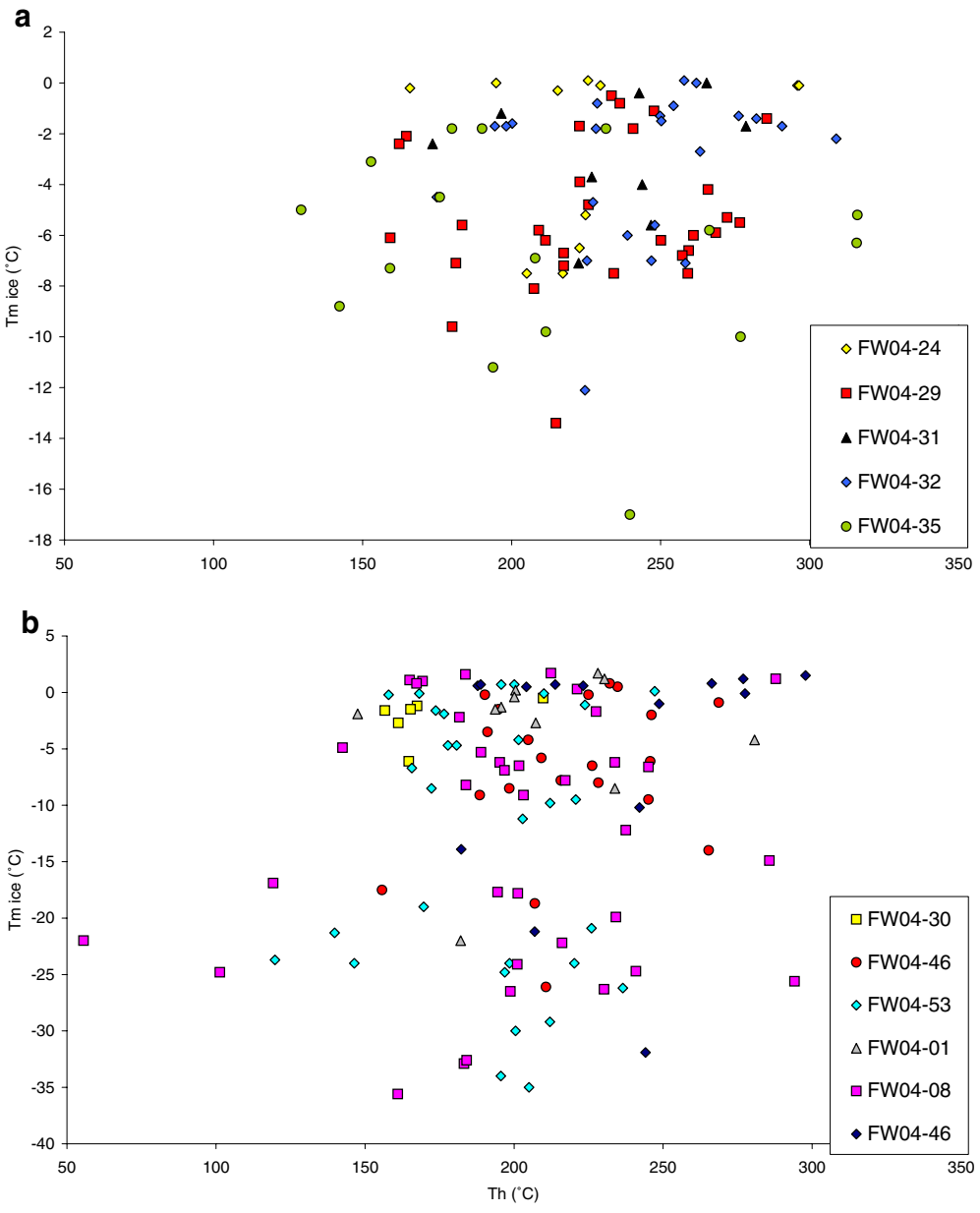

Fig. 12 **a** Homogenization temperatures vs final melting diagram of fluid inclusions in quartz. **b** Homogenization temperatures vs final melting diagram of fluid inclusions in calcite

inclusions. Barakat et al. (2002) interpreted the variations in salinity of the fluid inclusions in terms of a boiling process beneath the Bleïda gold deposit. Boiling can produce variations in salinity of fluids and variable proportion of volatiles being trapped in fluid inclusions. Therefore, the boiling model by Barakat et al. (2002) has some merits. However, the variation in salinity of quartz- and, especially calcite-hosted fluid inclusions may also be interpreted as mixing of hot, low-salinity hydrothermal fluids from depth with colder, saline formation waters that have achieved high salt content by dissolution of saline layers in the overlying strata. The current account on fluid inclusion data is equivocal and allows both interpretations.

Summary and discussion

The Bleïda Far West mineralization represents a new deposit type in the Anti-Atlas of Morocco. At Bleïda FW, gold–palladium mineralization is hosted by dominantly brittle structures and displays open-space filling textures in hydrothermally altered amphibolites and chlorite schists. The mineralization occurs in a corridor about 10×7 km wide and is associated with intense silicification and numerous, narrow, quartz-dominated, carbonate-bearing veins, which are parallel to the penetrative S2 foliation. A number of ore zones were proven to depths of at least 100 m. The ore lodes commonly occupy structurally favorable S2 sites in folded and sheared mylonitic bands. Individual veins are generally narrow (1–2 cm, locally up to 0.5 m wide) and are discontinuous along strike and down dip. The position of the ore-bearing structures indicates

that, in principle, the timing of the mineralization is synchronous with or later than B2, the second minor Pan-African event (ca. 605 Ma; Gasquet et al. 2005). This wide time interval illuminates the problems of the timing of mineralization in the Anti-Atlas of Morocco. For example, the silver ores of the Imiter deposit were emplaced at 550 Ma (Cheilletz et al. 2002; Levresse et al. 2004), whereas the gold mineralization of Iourirne was dated at ca. 300 Ma (Gasquet et al. 2004). Regarding the Co–As ores of Bou Azzer, Levresse (2001) gives a maximum mineralization age of 533±2 Ma (Aghbar trachyte, which predates the mineralization). Ledent (1960) arrived at an age of 240± 10 Ma (Pb/Pb) on syn-mineralization brannerite (which we recalculated to ca. 325 Ma), whereas En-Naciri et al. (1997) report a SIMS U/Pb isotope age of ca. 550 Ma for brannerite. Finally, Levresse (2001) obtained an age of 215±8 Ma using the Ar/Ar method on adularia from filon 7, Bou Azzer mine.

Obviously, regarding their absolute timing, the various mineralization in the Anti-Atlas (1) appear to have been polyphase, (2) their reported formation may have taken place over the wide time range from the Cambrian to the Triassic, and (3) most ages of mineralization are not at all well-constrained. Equally, indications toward the timing of the formation of gold mineralization at Bleïda FW are still vague. Barakat et al. (2002) propose a magmatic intrusion related to PIII volcanism as a heat source for the hydrothermal system and thus a late Pan-African age (~600–550 Ma) for the gold mineralization at Bleïda FW. However, Gasquet et al. (2005) also report hydrothermal activity in the Anti-Atlas at ~330–300 Ma related to the Variscan orogeny. One can speculate that this event may represent an alternative candidate for the mineralization at Bleïda FW. Future open pit mining will probably provide a better insight into the structural relationships and access to datable material to better constrain the timing of the mineralization.

The Bleïda FW mineralization is virtually sulfide-free. Gold is associated with abundant hematite, calcite, quartz, barite, epidote, and chlorite. Gold is silver- and palladium-bearing (up to 19 wt% Ag and 6.3 wt% Pd) and is intergrown with a distinct suite of PGM, namely mertieite-I/isomertieite, keithconnite, palladseite, and sperrylite. Secondary PGM formed by weathering are ill-defined phases or mixtures of Pd, Bi, V, Cu, Fe, and/or Mn oxides/hydroxides. Close to the surface, the mineralization is present as weathered, soft, clayey, and powdery material rich in Mn and Fe oxides/hydroxides with visible gold.

On a worldwide scale, similar gold–palladium mineralization associated with oxides (hematite) instead of sulfides as present at Bleïda FW is unusual and rare. For nearly two centuries, palladian gold was considered an exclusive feature of gold mineralization in banded iron formation in Brazil, and this type of mineralization was regarded as unique and was restricted to deposits in Brazil (e.g., Gehlen 1811; Hussak 1904; Clark et al. 1974; Jedwab and Cassedanne 1998). The "jacutinga" ores of the Quadrilátero Ferrífero, Minas Gerais are associated with hematite-rich veins that formed from hydrothermal, oxidizing fluid systems under relatively low-pressure conditions (Cabral et al. 2002c; Lüders et al. 2005; Cabral 2006). The ores also contain selenides such as palladseite (Davis et al. 1977; Cabral et al. 2002b,c) and generally show a geochemical signature comprising Au–Pd–As–Sb–Hg–Se–Te. Interestingly, as noted by Guimarães (1970), Varajão et al. (2000), and Cabral (2006), the Brazilian Au–Pd "jacutinga" ores seem to be associated with the last deformational event of the Brazilian–Pan African orogeny (750–450 Ma). Lüders et al. (2005) further constrain the age of mineralization to ca. 700–600 Ma.

During preceding decades, further Au–Pd occurrences and ores were reported from the Serra Pelada in Brazil (Meireles et al. 1982; Moroni et al. 2001; Şener et al. 2002; Cabral et al. 2002a,b; Cabral 2006), from the unconformity-related uranium deposits in the Northern Territory of Australia (Jabiluka, Coronation Hill, and Gold Ridge; Wilde et al. 1989; Carville et al. 1990; Şener et al. 2002), and from Hope's Nose and other localities in Devon, UK (e.g., Clark and Criddle 1982; Shepherd et al. 2005).

Cabral (2006) summarizes that the Brazilian Au–Pd ores (Gongo Soco, Itabira, and Serra Pelada) have the following features in common: (1) coarse-grained palladian gold, (2) abundant hematite, (3) sulfide-poor ore mineral assemblage, (4) a Au–Pd–As–Sb–Se–Hg signature, (5) dominantly brittle ore-hosting structures, and (6) open-space filling ore textures. Moderately to strongly saline, oxidized fluids deposited the mineralization at low (<300°C) temperatures (Cabral 2006), probably during the Brasiliano orogeny in Minas Gerais (700–600 Ma; Lüders et al. 2005).

The deposits of the Alligator Rivers field in the Northern Territory of Australia (Jabiluka, Coronation Hill, and Gold Ridge) are situated in Proterozoic sediments and show a distinct Au–PGE–selenide association with noble metal relations being Au>Pd>Pt (Wilde et al. 1989; Carville et al. 1990; Şener et al. 2002). At Coronation Hill, calcium-rich, highly oxidizing, low-pH brines deposited the mineralization at temperatures of about 140°C (Mernagh et al. 1994; Şener et al. 2002). Alteration assemblages with hematite and anatase in the mineralization of the Alligator Rivers field indicate the ingress of a relatively oxidized fluid, and temperatures between 150 and 200°C during mineralization and alteration were suggested by Wilde et al. (1989). Furthermore, an oxidized, slightly acidic, chloride-rich solution is envisaged as the most likely ore-transporting medium in which Au, Pd, Pt, Se, and Te were transported as chloride complexes (Wilde et al. 1989, Wilde 2005). Based on thermodynamic calculations, the authors also remark that high oxygen fugacities favor stabilization of selenides and tellurides of Pt and Pd preferentially to sulfides. A probable mineralization age of 1625±25 Ma was obtained on primary uranium ore of the Alligator Rivers field. Textural studies indicate that gold deposition overlapped with uraninite mineralization (Wilde et al. 1989).

European examples of gold–palladium occurrences comprise the unconformity-related, Triassic to early Jurassic (258–190 Ma) mineralization in South Devon,

UK (e.g., Clark and Criddle 1982; Gunn and Styles 2002; Shepherd et al. 2005). Shepherd et al. (2005) summarize that the distinctive features of the Devon red bed gold are the general absence of sulfide minerals, presence of selenides sometimes in association with tellurides and arsenides, and a pronounced enrichment in palladium. Au–Pd mineralization is hosted in carbonate veins with hematite and formed at low temperatures (86±13°C) from oxidizing sodic brines (Shepherd et al. 2005). Oxygen and carbon isotope studies of carbonates revealed the interaction of a saline and a lower salinity fluid in mineral deposition (Shepherd et al. 2005). The mineralization has a geochemical signature comprising Au–Pd–Se–As–Te.

Finally, mention must be made of gold and PGE contents of the Kupferschiefer in Poland and Germany. Kucha (1982) was the first to describe extraordinary enrichments of Au, Pt, and Pd in a thin bituminous layer at the base of the Zechstein black shale unit, and Oszczepalski et al. (1999) proved an extensive Au–PGE mineralization in intimate association with barren, red-colored rocks ("Rote Fäule") in the vicinity of the copper ores in the Lubin district of Poland. It is suggested that the precious metals were transported in oxidizing, slightly acidic, chloride brines derived from underlying red beds (Shepherd et al. 2005).

Our stable isotope and fluid inclusion studies corroborate and extend the findings of Barakat et al. (2002), who interpreted the variations in salinity of the fluid inclusions in terms of a boiling process beneath the Bleïda gold deposit. Boiling can produce variations in salinity of fluids and variable proportion of volatiles being trapped in fluid inclusions. However, the variation in salinity of quartz- and, especially, calcite-hosted fluid inclusions may also be interpreted as mixing of hot, low-salinity hydrothermal fluids from depth with colder, saline formation waters. The current account on fluid inclusion data is equivocal and allows both interpretations. However, in accordance with the observations on Au–Pd deposits in Brazil, Australia, and the UK, the Bleïda FW hydrothermal fluids also contained a chloride-rich, saline component oxidized and deposited at temperatures below 300°C.

In conclusion, common characteristics of Au–Pd mineralization worldwide are dominantly brittle ore-hosting structures, commonly in sediments of various ages. Sulfide-poor ore mineral assemblages and, at the same time, presence of abundant hematite, barite or gypsum, and selenides indicate mineral deposition from oxidizing fluids or brines with elevated chloride contents. Mineralization temperatures were generally in the epithermal range between 100 and 300°C. The ambient conditions of mineralization [low temperatures, low pH, elevated $f\,O_2$ (stability of hematite at 300°C at log $f\,O_2$ between −25 to −30; Pd and Pt selenides at 200°C at log $f\,O_2$ between about −29 and −37), distinct chloride contents of the fluids] favor a transport of gold in the form of chloride complexes (Wilde et al. 1989). The same applies for the PGE, as significant PGE transport by chloride is possible if certain chemical requirements at low temperatures (high $f\,O_2$, low pH, or both) are met (Wilde et al. 1989; Hanley 2005).

Au–Pd mineralization is further characterized by noble metal abundances in the order Au>Pd>Pt and association of the mineralization with the heavier elements of main groups Va (i.e., As–Sb–Bi) and VIa (i.e., Se–Te) of the periodic table, generally reflected by the chemical signature Au–Pd–Se–Te (±As, ±Sb, ±Bi). As such, the Au–Pd association represents a discrete style of mineralization (the epithermal gold–selenide class of Lindgren 1928), distinct from the sulfide-bearing epithermal gold deposits (e.g., Sillitoe (1993) and also the larger and well-known group of sulfide-bearing, generally reduced mesothermal or orogenic gold deposits (e.g., Colvine et al. 1988; Groves et al. 1998; Goldfarb et al. 2001).

Conclusions

1. At Bleïda Far West, structurally controlled gold–palladium mineralization is hosted by dominantly brittle B2 structures and open-space filling textures in hydrothermally altered amphibolites and chlorite schists.
2. Suggestions toward the timing of the formation of gold mineralization are vague. Structural observations indicate that the mineralization was synchronous with or later than the minor Pan-African B2 tectonic event (ca. 605 Ma). It is still speculative whether the Bleïda FW mineralization is late Pan-African (~600–550 Ma; Barakat et al. 2002), connected with the Variscan orogeny (~330–300 Ma; Gasquet et al. 2005), or related to some other hydrothermal event.
3. The mineralization is virtually sulfide-free. Instead, free gold is associated with abundant hematite, calcite, quartz, barite, epidote, and chlorite.
4. The gold grains are silver- and palladium-bearing (up to 19 wt% Ag and 6.3 wt% Pd) and are intergrown with a distinct suite of PGM, namely mertieite-I/isomertieite, keithconnite, palladseite, and sperrylite (chemical signature mainly Au–Pd–As–Sb–Se–Te).
5. Stable isotope and fluid inclusion studies indicate fluid development with time or mixing of two fluids with a prominent saline component in the ore-forming fluids. In conjunction with the mineral association, oxidizing fluids are indicated, and Au and PGE transport and deposition took place by chloride complexes in the epithermal range, at elevated $f\,O_2$ and/or low pH.
6. Common to all Au–Pd mineralization worldwide is their formation in the epithermal (<300°C) range; deposition mainly in brittle structures; sulfide-poor mineral assemblages with hematite; sulfate minerals, and selenides; and metal transport by and deposition from oxidized, chloride-rich fluids. Au–Pd mineralization is further characterized by noble metal abundances in the order Au>Pd>Pt and the chemical signature Au–Pd–Se–Te (±As, ±Sb, ±Bi). As such, the Au–Pd association represents a discrete style of gold mineralization distinct from other epigenetic gold ores.

Acknowledgements We acknowledge assistance in the field given by the Managem and Reminex Companies of Groupe ONA. Many thanks for their continuous help go to our colleagues in the Bou Azzer mining district. M. El G. obtained financial support through a grant in the "sandwich program" of the German Academic Exchange Service (DAAD). The authors are grateful to the BGR for supporting the studies of the first author, and special thanks go to T. Malarski for the preparation of excellent polished sections, D. Klosa for SEM work, and J. Lodziak for performing the microprobe analyses. We are grateful for the comments of the reviewers Alexandre Cabral, Alain Cheilletz, and the Editor, Bernd Lehmann, which considerably stream-lined and focused the paper.

References

Bakker RJ, Dubessy J, Cathelineau M (1996) Improvements in clathrate modelling I: the H_2O–CO_2 system with various salts. Geochim Cosmochim Acta 60:1657–1681

Barakat A, Marignac C, Boiron M-C, Bouabdelli M (2002) Caractérisation des paragenèses et des paléocirculations fluides dans l'indice d'or de Bleïda (Anti-Atlas, Maroc). Comptes Rendu Geosciences 334:35–41

Barnes HL (1979) Geochemistry of hydrothermal ore deposits, 2nd edn. Wiley, New York, p 798

Barnes HL (1997) Geochemistry of hydrothermal ore deposits, 3rd edn. Wiley, New York, p 972

Barton PB, Chou IM (1993) Refinement of the evaluation of the role of CO_2 in modifying estimates of the pressure of epithermal mineralization. Econ Geol 88:873–884

Borthwick J, Harmon RS (1982) A note regarding ClF_3 as an alternative to BrF_5 for oxygen isotope analyses. Geochim Cosmochim Acta 46:1665–1668

Cabral AR (2006) Palladian gold mineralization (*ouro preto*) in Brazil: Gongo Soco, Itabira and Serra Pelada. Geol Jahrb Reihe D Sonderheft 8 (in press)

Cabral AR, Lehmann B, Kwitko R, Cravo Costa CH (2002a) The Serra Pelada Au–Pd–Pt deposit, Carajás mineral province, northern Brazil: reconnaissance mineralogy and chemistry of very high grade palladian gold mineralization. Econ Geol 97:1127–1138

Cabral AR, Lehmann B, Kwitko-Ribeiro R, Cravo Costa CH (2002b) Palladium and platinum minerals from the Serra Pelada Au–Pd–Pt deposit, Carajás mineral province, northern Brazil. Can Mineral 40:1451–1463

Cabral AR, Lehmann B, Kwitko R, Galbiatti HF, Pereira MC (2002c) Palladseite and its oxidation: evidence from palladian gold vein-type mineralization (jacutinga), Cauê iron-ore mine, Quadrilátero Ferrífero, Minas Gerais, Brazil. Mineral Mag 66:327–336

Cabri LJ (2002) The platinum group minerals. In: Cabri LJ (ed) The geology, geochemistry, mineralogy and mineral beneficiation of platinum group element. Canadian Institute of Mining, Metallurgy and Petroleum, special vol. 54. p 13-130

Carville DP, Leckie JF, Moorhead CF, Rayner JG, Durbin AA (1990) Coronation Hill gold–platinum–palladium deposit. In: Hughes FE (ed) Geology of the mineral deposits of Australia and Papua New Guinea. Australasian Institute of Mining and Metallurgy, Melbourne, pp 759–762

Cheilletz A, Levresse G, Gasquet D, Azizi Samir MR, Zyadi R, Archibald DA (2002) The Imiter epithermal deposit (Morocco): new petrographic, microtectonic and geochronological data. Importance of the Precambrian–Cambrian transition for major precious metal deposits in the Anti-Atlas. Miner Depos 37:772–782

Choubert G (1963) Histoire Géologique du Précambrien de l'Anti-Atlas. Notes & Mém Serv Geol Maroc 162:7–352

Clark AM, Criddle AJ (1982) Palladium minerals from Hope's Nose, Torquay, Devon. Mineral Mag 46:371–377

Clark AM, Criddle AJ, Fejer EE (1974) Palladium arsenide–antimonides from Itabira, Minas Gerais, Brazil. Mineral Mag 39:528–543

Clauer N (1976) Géochimie isotopique du strontium des milieux sédimentaires. Application à la géochronologie de la couverture du craton ouest-africain. Ph.D. Thesis, University of Strasbourg, p 256

Colvine AC, Fyon JA, Heather KB, Marmont S, Smith PM, Troop DG (1988) Archean lode gold deposits in Ontario. Ont Geol Surv Misc Pap 139:136

Daltry VDC, Wilson AH (1997) Review of platinum-group mineralogy: Compositions and elemental associations of the PG-minerals and unidentified PGE-phases. Mineral Petrol 60:185–229

Davis RJ, Clark AM, Criddle AJ (1977) Palladseite, a new mineral from Itabira, Minas Gerais, Brazil. Mineral Mag 41:10–13

En-Naciri A, Barbanson L, Touray JC (1997) Brine inclusions from the Co–As(Au) Bou Azzer district, Anti-Atlas, Morocco. Econ Geol 92:360–367

Gasquet D, Chèvremont P, Baudin T, Chalot-Prat F, Guerrot C, Cocherie A, Roger J, Hassenforder B, Cheilletz A (2004) Polycyclic magmatism in the Tagragra and Kerdous-Tafeltast inliers (western Anti-Atlas, Morocco). J Afr Earth Sci 39:267–275

Gasquet D, Levresse G, Cheilletz A, Azizi-Samir MR, Mouttaqi A (2005) Contribution to a geodynamic reconstruction of the Anti-Atlas (Morocco) during Pan-African times, with the emphasis on inversion tectonics and metallogenic activity at the Precambrian–Cambrian transition. Precamb Res 140:157–182

Gehlen AF (1811) Platin und Palladium in Brasilien und St. Domingo gefunden. J Chemie Physik 1:362–373

Goldfarb RJ, Groves DI, Gardoll S (2001) Orogenic gold and geologic time: a global synthesis. Ore Geol Rev 18:1–75

Groves DI, Goldfarb RJ, Gebre-Mariam M, Hagemann SG, Robert F (1998) Orogenic gold deposits: a proposed classification in the context of their crustal distribution and relationship to other gold deposit types. Ore Geol Rev 13:7–27

Guimarães D (1970) Arqueogênese do ouro na regiaõ central de Minas Gerais. DNPM/DFPM, Rio de Janeiro, Boletim 139, p 51

Gunn AG, Styles MT (2002) Platinum-group element occurrences in Britain: magmatic, hydrothermal ans supergene. Trans Inst Min Metall 307:B2–B14

Hanley JJ (2005) The aqueous geochemistry of the platinum-group elements (PGE) in surficial, low-T hydrothermal and high-T magmatic–hydrothermal environments. In: Mungall J (ed) Exploration for platinum-group element deposits, Mineral Ass Canad Short Course 35:35–56

Hefferan K, Karson JA, Saquaque A (1992) Proterozoic collisional basins in a Pan-African suture zone, Anti-Atlas Mountains, Morocco. Precamb Res 54:295–319

Hefferan K, Admou H, Karson JA, Saquaque A (2000) Anti-Atlas (Morocco) role in Neoproterozoic Western Godwana reconstruction. Precamb Res 103:89–96

Hefferan K, Admou H, Hilal R, Karson JA, Saquaque A, Juteau T, Bohn M, Samson SD, Kornprobst J (2002) Proterozoic blueschist-bearing mélange in the Anti-Atlas Mountains, Morocco. Precamb Res 118:179–194

Hussak E (1904) Über das Vorkommen von Platin und Palladium in Brasilien. Sitzungsber Kaiserl Akad Wiss 113:379–468

Inglis JD, MacLean JS, Samson SD, D'Lemons RS, Admou H, Hefferan K (2004) A precise U–Pb zircon age for the Bleïda granodiorite, anti-Atlas, Morocco: implications for the timing of deformation and terrane assembly in the eastern Anti-Atlas. J Afr Earth Sci 39:277–283

Jedwab J, Cassedanne J (1998) Historical observations on oxygen-bearing compounds of platinum and palladium in Minas Gerais, Brazil. Can Mineral 36:887–893

Kerrich R (1987) The stable isotope geochemistry of Au–Ag vein deposits in metamorphic rocks. In: Kyser TK (ed) Stable isotope chemistry of low temperature fluids. Min Ass Canad Short Course 13:287–336

Kucha H (1982) Platinum-group metals in the Zechstein copper deposits, Poland. Econ Geol 77:1578–1591
Kyser TK (1987) Stable isotope chemistry of low temperature fluids. Min Ass Canad Short Course 13:452
Leblanc M (1981) ophiolites précambiennes et gîtes arséniés de Cobalt (Bou Azzer–Maroc). Notes et mémoires du service géologique du Maroc, N°280, p 306, plus maps
Leblanc M, Billaud P (1978) A volcano-sedimentary copper deposit on a continental margin of upper Proterozoic age: Bleïda (Anti-Atlas, Morocco). Econ Geol 73:1101–1111
Leblanc M, Lancelot J (1980) Interprétation géodynamique du domaine panafricain de l'Anti-Atlas (Maroc) à partir de données géologiques et géochronologiques. Can J Earth Sci 17:142–155
Leblanc M, Moussine-Pouchkine A (1994) Sedimentary and volcanic evolution of a Neoproterozoic continental margin (Bleida, Anti-Atlas, Morocco). Precamb Res 70:25–44
Ledent D (1960) Age absolu d'une brannérite de Bou–Azzer (Sud-Marocain). Académie des Sciences Belgique, Brussels, pp 1309–1311
Levresse G (2001) Contribution à l'établissement d'un modèle génétique des gisements d'Imiter (Ag–Hg), Bou Madine (Pb–Zn–Cu–Ag–Au) et Bou Azzer (Co–Ni–As–Ag–Au) dans l'Anti-Atlas marocain. Ph.D. thesis, CRPG-CNRS Nancy, France, p 191
Levresse G, Cheilletz A, Gasquet D, Reisberg L, Deloule E, Marty B, Kyser K (2004) Osmium, sulphur, and helium isotopic results from the giant Neoproterozoic epithermal Imiter silver deposit, Morocco: evidence for a mantle source. Chem Geol 207:59–79
Lindgren W (1928) Mineral deposits. McGraw Hill, New York, p 1049
Locmelis M (2005) The mineralogical siting of platinum-group elements in the oxidized main sulfide zone at Hartley Mine, Great Dyke, Zimbabwe. BGR Internal Report No 11694/05:95 (plus Appendices)
Lüders V, Romer RL, Cabral AR, Schmidt C, Banks DA, Schneider J (2005) Genesis of itabirite-hosted Au–Pd–Pt-bearing hematite-(quartz) veins, Quadrilátero Ferrífero, Minas Gerais, Brazil: Constraints from fluid inclusion infrared microthermometry, bulk crush-leach analysis and U–Pb systematics. Miner Depos 40:289–306
Makovicky E (2002) Ternary and quaternary phase systems with PGE. In: LJ Cabri (ed) The geology, geochemistry, mineralogy and mineral beneficiation of platinum-group elements. Canadian Institute of Mining, Metallurgy and Petroleum, special vol. 54, pp 131–175
McCrea JM (1950) On the isotopic chemistry of carbonates and a paleotemperature scale. J Chem Physics 18:849–857
Meireles E de M, Teixeira JT, Medeiros Filho CA (1982) Geologia preliminary do depósito de ouro de Serra Pelada. In: Sympósio de Geologia da Amazônia, Belém, vol. 2, pp 74–83
Mernagh TP, Heinrich CA, Leckie JF, Carville DP, Gilbert DJ, Valenta RK, Wyborn LAI (1994) Chemistry of low-temperature hydrothermal gold, platinum and palladium (± uranium) mineralization at Coronation Hill, Northern Territory, Australia. Econ Geol 89:1053–1073
Moroni M, Girardi VAV, Ferrario A (2001) The Serra Pelada Au–PGE deposit, Serra dos Carajás /Pará State, Brazil): Geological and geochemical indications for a composite mineralizing process. Miner Depos 36:768–785
Mouttaqi A, Sagon JP (1999) Le gisement de cuivre de Bleida (Anti-Atlas central): une interférence entre les processus de remplacement et d'exhalaison dans un contexte de rift. Chron Rech Min 536–537:5–21
Oberthür T, Melcher F (2005) Behaviour of PGE and PGM in the supergene environment: a case study of persistence and redistribution in the main sulphide zone of the Great Dyke, Zimbabwe. In: Mungall J (ed) Exploration for platinum-group element deposits. Mineral Ass Canad Short Course 35:97–111
Ohmoto H, Goldhaber MB (1997) Sulfur and carbon isotopes. In: Barnes HL (ed) Geochemistry of hydrothermal ore deposits. Wiley, New York, pp 517–600
Olivo GR, Gauthier M (1995) Palladium minerals from the Cauê iron mine, Itabira District, Minas Gerais, Brazil. Mineral Mag 59:457–465
Oszczepalski S, Rydzewski A, Speczik S (1999) Rote Fäule-related Au–Pt–Pd mineralization in SW Poland: new data. In: Stanley et al (ed) Mineral deposits: processes to processing. Balkema, Rotterdam, pp 1423–1425
Roedder (1984) Fluid inclusions. Rev Miner 12:1–644
Rollinson H (1993) Using geochemical data: evaluation, presentation, interpretation. Longman, p 352
Saquaque A, Admou H, Karson J, Hefferan K, Reuber I (1989) Precambrian accretionary tectonics in the Bou Azzer–El Graara region, Anti-Atlas, Morocco. Geology l7:1107–1110
Saquaque A, Benharref M, Abia H, Mrini Z, Reuber I, Karson J (1992) Evidence for a Pan-African volcanic arc and wrench fault tectonics in the Jbel Saghro, Anti-Atlas, Morocco. Geol Rundsch 81:1–13
Şener AK, Grainger CJ, Groves DI (2002) Epigenetic gold–platinum-group element deposits: examples from Brazil and Australia. Trans Inst Min Metall 307:B65–B73
Shepherd TJ, Bouch JE, Gunn AG, McKervey JA, Naden J, Scrivener RC, Styles MT, Large DE (2005) Permo–Triassic unconformity-related Au–Pd mineralization, South Devon, UK: new insights and the European perspective. Miner Depos 40:24–44
Sillitoe RH (1993) Epithermal models: genetic types, geometric controls and shallow features. Geol Assoc Can Special Volume 40:403–417
Thomas RJ, Fekkak A, Ennih N, Errami E, Loughlin ES, Gresse PG, Chevallier LP, Liégois JP (2004) A new lithostratigraphic framework for the Anti-Atlas orogen, Morocco. J Afr Earth Sci 39:217–226
Tolstykh ND, Sidorov EG, Laajoki KVO, Krivenko AP, Podlipskiy M (2000) The association of platinum-group minerals in placers of the Pustaya River, Kamchatka, Russia. Can Mineral 38:1251–1264
Varajão CAC, Colin F, Vieillard P, Melfi AJ, Nahon D (2000) Early weathering of palladium gold under lateritic conditions, Maquiné Mine, Minas Gerais, Brazil. Appl Geochem 15:245–263
Wilde AR (2005) Descriptive ore deposit models: Hydrothermal and supergene Pt & Pd deposits. In: Mungall J (ed) Exploration for platinum-group element deposits. Mineral Ass Canad Short Course 35:145–161
Wilde AR, Bloom MS, Wall VJ (1989) Transport and deposition of gold, uranium, and platinum-group elements in unconformity-related uranium deposits. In: Keays RD, Ramsay WRH, Groves DI (eds) The geology of gold deposits—the perspective in 1988. Econ Geol Monogr 6:637–650